JOURNAL OF HEAVY METAL RESEARCH

https://jhmr.hsu.ac.ir E-ISSN: 3116-0522 Journal of Heavy Metal Research, 2026, vol 1, Issue 3, 1-17

Original Article

Geochronology and zircon geochemistry of Mn-hosting tuffaceous sequences in the Southern Sabzevar, NE Iran

Seyed Ali Mazhari[1,2]*

1. Research Center of Geographical Sciences and Social Studies, Hakim Sabzevari University, Sabzevar, Iran,
2. Heavy Metals Research Center, University of Hakim Sabzevari, Sabzevar, Iran

* Correspondence: a.mazhari@hsu.ac.ir

Received: 10 August 2026
Revised: 17 September 2026
Accepted: 28 September 2026
Published: 30 September 2026

Publisher: Hakim Sabzevari University

Citation: Mazhari, S.A. (2026). Geochronology and zircon geochemistry of Mn-hosting tuffaceous sequences in the Southern Sabzevar, NE Iran. *Journal of Heavy Metal Research, 1*(3), 1–17.

Authors retain the copyright and full publishing rights.

Copyright: Submitted for open access publication under the terms and conditions of the Creative Commons Attribution (CC BY 4.0) license.

Abstract

The manganese occurrences in southern Sabzevar are historically attributed to hydrothermal exhalative, Besshi-type volcanogenic massive sulfide (VMS) systems; however, the precise timing of volcanosedimentary accumulation and its geodynamic driver have remained poorly constrained. Here, we present in situ zircon U–Pb geochronology and trace-element geochemistry from tuffaceous units interbedded with these Mn-bearing successions. Zircons exhibit clear oscillatory zoning and high Th/U ratios (0.28–1.03), indicative of a primary magmatic origin. Weighted mean 206Pb/238U ages from four key localities, Landaran (102 ± 0.6 Ma), Bardashkand (104.2 ± 0.9 Ma), Kuhsakht (100.2 ± 0.8 Ma), and Siabkuh (99.6 ± 1.6 Ma), define a coherent mid-Cretaceous (ca. 104–100 Ma; Albian–Cenomanian boundary) maximum depositional age for the host volcaniclastic sequences and contemporaneous hydrothermal exhalative Mn mineralization. Subordinate inherited zircons yielding older ages (up to ~140 Ma) record the assimilation of earlier Mesozoic basement lithologies. Trace-element discrimination diagrams demonstrate that parental melts were predominantly generated within an oceanic island-arc regime, with subordinate within-plate components and localized continental crustal input in the Bardashkand sector. Combined with adjacent crustal evidence of fossil hydrothermal chimneys, spilitic alteration, and pervasive base-metal mineralizations, our findings demonstrate that ore genesis took place within an evolving accretionary wedge–forearc–arc system rather than an isolated back-arc basin. Extensional rifting in this dynamic subduction-related realm promoted elevated geothermal gradients and seawater convection through permeable oceanic crust, culminating in the exhalative precipitation of stratiform Mn deposits on the paleo-seafloor.

Keywords: Southern Sabzevar; Zircon U–Pb geochronology; Zircon trace elements; Tuff; Manganese mineralization

1. Introduction

Manganese deposits associated with volcanic-sedimentary successions commonly represent important records of submarine hydrothermal activity, volcanism, basin development, and seawater–fluid interaction. In such settings, Mn may precipitate from hydrothermal plumes or diffuse fluids in association with siliceous, carbonate-rich, ferruginous, and volcaniclastic sediments. Their genesis may therefore be closely linked to

contemporaneous or near-contemporaneous volcanic activity, tectonic extension, crustal accretion, arc development, or the evolution of oceanic to marginal-basin environments (Karataş et al., 2022; Guo et al., 2024; Christin Natalia et al., 2024; Putzolu et al., 2025; Maghfouri et al., 2026).

The Sabzevar ophiolitic belt in northeastern Iran comprises tectonically dismembered remnants of an oceanic to supra-subduction-zone assemblage, together with associated volcano-sedimentary sequences and a variety of mineral occurrences, including manganese (Mn) mineralization (Maghfouri et al., 2016, 2017; Hashempour et al., 2023). In the southern part of the belt, Mn-bearing horizons are hosted within, or immediately adjacent to, tuffaceous carbonate and crystal-tuff units (Maghfouri et al., 2016). The occurrence of several stratiform, volcanogenic Mn deposits in this area (Maghfouri et al., 2017) points to a typical volcanic-hydrothermal, exhalative–diagenetic mineralization model, whereby Mn-bearing minerals precipitated as hydrothermal fluids vented into overlying dysoxic water columns (Hashempour et al., 2023).

Establishing the temporal relationship between volcanism, deposition of host rocks, and Mn mineralization is essential for reconstructing the metallogenic evolution of this area. Zircon is especially useful for this purpose because it can preserve magmatic crystallization ages and trace-element signatures through later sedimentary, hydrothermal, and metamorphic processes (Belousova et al. 2002; Grimes et al. 2007; Broska and Petrik, 2014; Zhong et al., 2021; Njinchuki et al., 2026). Zircon U–Pb geochronology may provide a robust age for an eruption when the analyzed grains are juvenile and directly related to volcanic ash deposition. However, in volcaniclastic or tuffaceous sedimentary successions, zircon ages may alternatively record the age of the magmatic source rather than the exact depositional age of the host sediment (Königer et al., 2002; Chakraborty et al., 2023). This distinction is especially important where volcaniclastic material may have been reworked after eruption or where the succession includes several stratigraphically distinct mineralized horizons (Brlek et al., 2021; Pupin, 2024; Calver et al., 2026).

Previous regional studies have suggested more than one Cretaceous magmatic episode in the southern Sabzevar region, including an older magmatic interval broadly between 110 and 90 Ma and a younger interval around 82–75 Ma (Kazemi et al., 2019; Mazhari et al., 2019; Mazhari and Bea, 2026). At the same time, some stratigraphic interpretations have assigned parts of the Mn-hosting succession to the Late Cretaceous (Maghfouri et al., 2017; Hashemipour et al., 2023).

Although field relationships in the southern Sabzevar area indicate that the tuffaceous units host, or are closely associated with, the Mn-bearing horizons, no precise geochronological data currently exist to constrain the timing of these volcaniclastic deposits and, consequently, the age of the associated manganese mineralization. This study addresses this gap by applying zircon U–Pb geochronology to the tuffaceous units. These data are intended to (i) constrain the depositional age of the tuffaceous host rocks and, by extension, the timing of the Mn mineralization, and (ii) characterize, through the trace-element and isotopic signatures of the same zircon populations, the magmatic affinity and tectonic setting of the volcanic source rocks. Collectively, these results aim to provide a revised temporal and geodynamic framework for the volcanosedimentary and metallogenic evolution of the Sabzevar ophiolitic belt.

2. Geological Background

The Sabzevar subzone in the northeastern Central-Eastern Iranian Microcontinent (CEIM) (Fig. 1a) is considered one of the oceanic basins surrounding Neotethys, whose complex geological history has undergone various stages of ocean basin opening, subduction, and tectonic plate collision (Omrani et al., 2018; Jafari and Ghasemi, 2023; Moghadam et al., 2025). The subzone comprises variable proportions of ultramafic rocks, gabbros, mafic volcanic rocks, volcaniclastic sequences, radiolarian-bearing sediments, carbonate units, and tectonically disrupted mélanges (Khalatbari Jafari et al., 2013; Moghadam et al., 2014).

The southern Sabzevar contains the largest exposure of Late Cretaceous rocks outside of the ophiolitic assemblage of the Sabzevar Subzone. In this region, a volcanic-sedimentary sequence (limestone and various tuffs) is characterized by a northeast-southwest orientation (Fig. 1b), comprising extrusive igneous rocks such as trachyandesite, dacite, and rhyolite, as well as semi-

deep intrusive rocks with gabbro, gabbro-diorite, diorite, and granite compositions, along with pyroclastic rocks (including various tuffs) (Kazemi, 2018). The igneous rocks of this region were formed during two time intervals, approximately 75 Ma and 98-101 Ma, and they exhibit similar Nd and Sr isotopic values, indicating a genetic relationship between them (Kazemi et al., 2019). Geochemical evidence suggests that the magma forming the igneous rocks originated from a depleted mantle wedge in a subduction environment during the subduction of the Neotethys oceanic basin in the Late Cretaceous period (Kazemi, 2018).

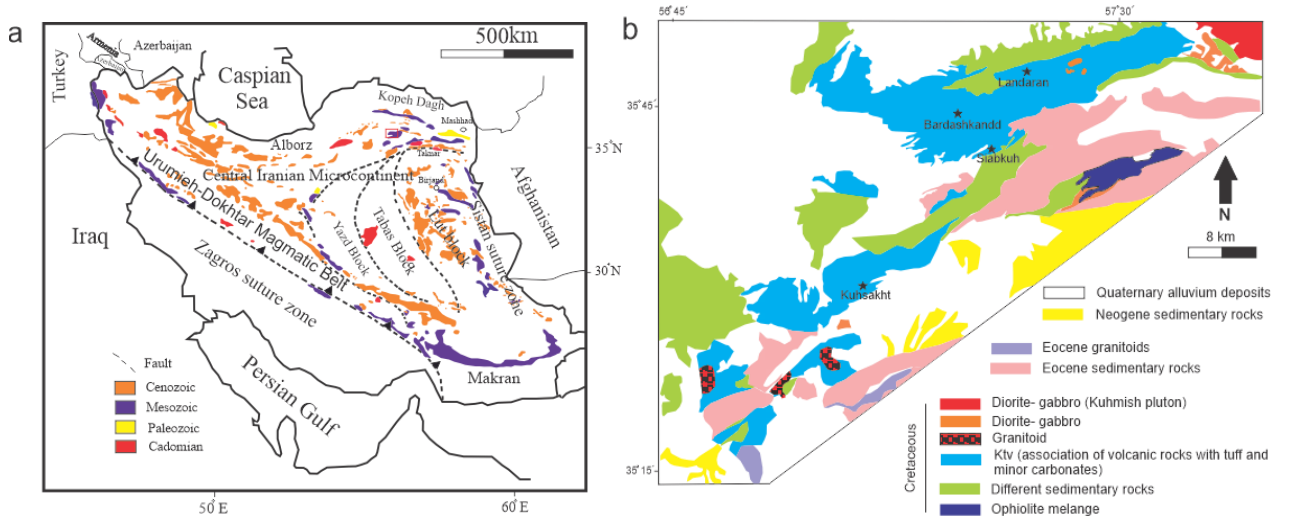

Figure1. (a) Location of the study area in the geological map of Iran (indicated by the red rectangle). (b) Geological map of the southern Sabzevar subzone, showing the locations of the studied mineralized zones.

In addition to the diversity of volcanic rocks and the sequence of sedimentary and volcaniclastic sedimentary rocks, the abundance of polymetallic deposits, particularly manganese and copper, has established the southern Sabzevar as a prominent hub for mineral exploration. The manganese deposit of Chashme Frezi, which includes several manganese reserves in this area, has been referred to as exhalative and Besshi-type volcanogenic massive sulfide deposits (Maghfouri et al., 2017). The manganese deposit of Cheshmeh Frezi is situated within a host rock composed of red tuff, which is interlayered with green tuffaceous sandstone from the Late Lower Cretaceous. The volcanic rocks of the Footwall and hanging wall are often andesite and trachy-andesite, exhibiting geochemical characteristics indicative of back-arc settings (Maghfouri et al., 2017). The manganese and copper reserves of Nudah, located near the Cheshmeh Frezi, exhibit similarities to the volcanic-type Besshi massive sulfide deposits. These reserves are situated within host rocks comprising alkaline olivine basalt and siliceous tufaceous sandstone (Maghfouri et al., 2016; Tashi et al., 2021). Based on structural and geochemical studies, the manganese deposits of Mohammadabad and Goft in the eastern part of this area exhibit distinct characteristics of volcanic hydrothermal exhalative-diagenetic type (Hashempour et al., 2023). The tectonic setting of manganese deposits in the southwest region of Sabzevar, based on geochemical investigations, is identified as a back-arc extensional environment (Hashemipour et al., 2023).

Field investigations in the studied prospects reveal an intimate spatial, stratigraphical, and genetic relationship between the volcaniclastic successions and manganese mineralization across southern Sabzevar (Figs. 2 and 3). In the Bardashkand prospect, the manganese ore body occurs predominantly within the basal sections of thick, well-developed columnarly jointed silicic tuffs (Figs. 2a, b), reflecting high-energy pyroclastic deposition followed by exhalative mineralization during volcanic quiescence. In contrast, the manganese mineralization in the Landaran area exhibits pronounced stratiform to manto-type geometries intercalated conformably within finely bedded tuffaceous horizons (Figs. 2c, d), indicating syngenetic deposition onto the seafloor. Furthermore, in the Siabkuh prospect, the manganese-bearing layers are tightly intertwined with green tuffs (Figs.

3a, b), displaying distinct bedding concordant with the volcaniclastic host rocks. In the Kuh-Sakht prospect, the mineralized carbonate tuff sequence is stratigraphically capped by a thick, massive limestone unit (Figs. 3c, d), pointing to a transitional volcano-sedimentary depositional setting evolving toward a shallow marine carbonate platform. Collectively, these macroscopic and field-structural relationships substantiate that the episodic explosive volcanism and resulting diverse tuffaceous sequences not only provided the primary physical host for the ore-forming hydrothermal fluids, but also constrained the spatial distribution and geometric styles of the manganese deposits in the region.

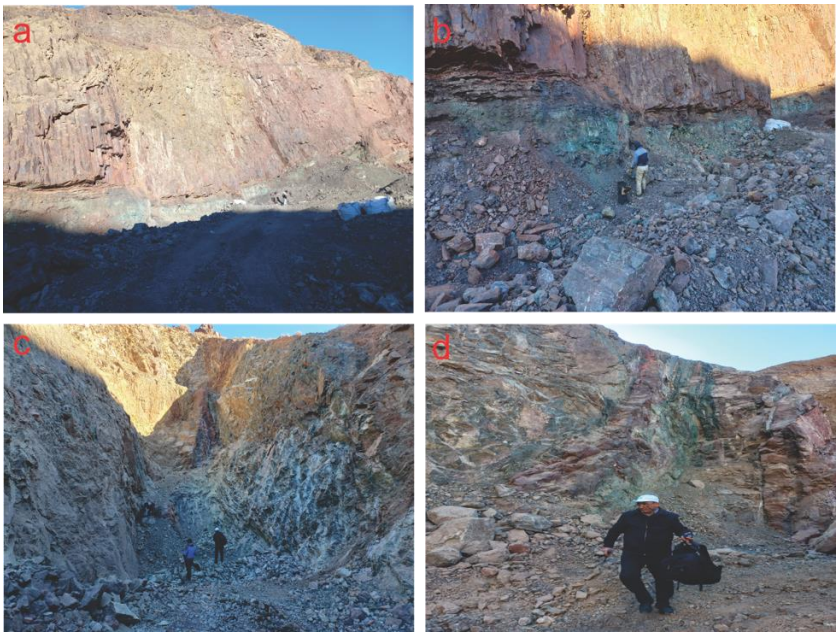

Figure 2. Field relationships between the studied tuffs and manganese-bearing veins in the Bardashkand (a, b) and Landaran (c, d) prospects. (a) The manganese ore body in Bardashkand is hosted within the lower parts of thick, columnarly jointed silicic tuffs, with a close-up view shown in (b). In the Landaran prospect, stratiform/manto-type manganese veins are intercalated within the tuffs; (c) and (d) present panoramic and close-up views, respectively.

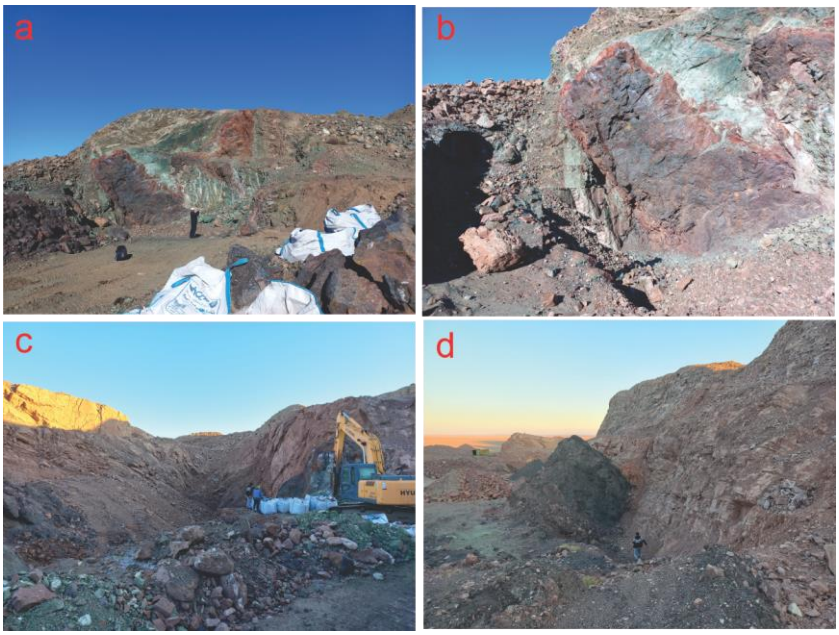

Figure 3. Field relationships of manganese mineralization in the studied areas: (a) overview and (b) detailed view of the manganese-bearing layers hosted within green tuffs in the Siabkuh prospect. (c, d) Manganese-mineralized carbonate tuff underlying a thick limestone sequence in the Kuh-Sakht prospect, showing (c) panoramic and (d) close-up exposures.

3. Materials and Methods

Four Mn-associated tuffaceous horizons from the southern Sabzevar area, namely the Landaran, Siabkuh, Kuhsakht, and Bardashkand localities (Fig. 1b), were sampled for this study. The collected lithologies consist of acidic crystal tuff and lithic tuff.

Zircon separation was performed using hand panning, first in water and subsequently in ethanol. In the next steps, magnetic separation was applied to remove iron-rich minerals, followed by final hand-picking under a binocular microscope. The zircon grains were analyzed using a SHRIMP IIe/MC instrument, following the procedure described by Williams and Claesson (1987). The analytical routine involved beam sputtering for 120 seconds and the acquisition of six scans with specific isotopic sequences. The operating conditions included a primary beam of 5 nA and a mass resolution of 5000. Calibration was performed using the REG and SL13 standards (for concentration) and the TEMORA standard (for isotopic ratios), which were measured once every four samples. Analytical procedures and error calculations are detailed in Mazhari and Klötzli (2023). Isotopic uncertainties are reported at the one-sigma level, whereas age uncertainties are given at the two-sigma level.

Trace-element analyses of the zircon grains were carried out using an Agilent 7500 quadrupole ICP-MS coupled with a Nd:YAG Mercantek laser-ablation system operating at 213 nm wavelength in a helium atmosphere. The operating conditions of both the laser and the ICP-MS, as well as the of both the laser and the ICP-MS, as well as the data-reduction scheme, follow those described by Liang et al. (2009) density was 8.5 J/cm². All spot analyses were performed at a repetition rate of 10 Hz. NIST SRM 610 and TEMORA 2 (TEM) were used as external standards, while ^{29}Si served as the internal standard. To evaluate data quality, the trace-element composition of hydrothermal zircon crystals from sample B1-10 was independently determined using both NIST SRM 610 and SRM 612 as external standards. All laser-ablation spots were carefully selected to avoid mineral and melt inclusions, as well as cracks within the zircon grains; only smooth LA-ICP-MS signals were considered for analysis. Following acquisition, integration of background and analytical signals, correction for time-dependent drift, and quantitative calibration for trace elements were computed using the GLITTER 4.0 software package (Macquarie University). The concentrations of titanium and rare-earth elements (REEs) in the analyzed samples were three orders of magnitude above the instrumental detection limits, and the relative analytical uncertainties were less than 5%.

4. Results and discussion

4.1. Zircon morphology and internal textures

The analyzed zircons are predominantly euhedral to subhedral (Fig. 4). Their preserved crystal forms and the general absence of dominant rounded or strongly abraded grains support a primary magmatic or volcanogenic origin. Cathodoluminescence images reveal well-developed oscillatory zoning in most grains (Fig. 4), which is characteristic of zircon crystallized from magmatic melts (Corfu et al., 2003).

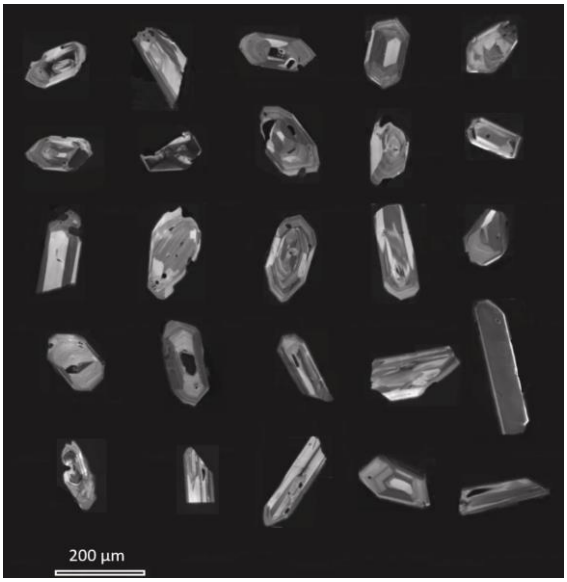

Figure 4. Representative cathodoluminescence (CL) images of zircons separated from the studied tuffs. Most crystals exhibit euhedral to subhedral, prismatic, and pyramidal morphologies with well-developed oscillatory magmatic zoning, indicating a primary igneous origin with little or no inherited core. The scale bar is 200 µm.

The observed textures do not indicate that hydrothermal zircon growth, widespread dissolution–reprecipitation, or extensive recrystallization dominates the analyzed population. Although minor alteration along cracks, grain boundaries, or rims cannot be excluded

without detailed imaging and spot-by-spot chemical comparison, the overall zircon population retains a dominantly magmatic internal structure.

4.2. U–Pb geochronology

The U–Pb geochronological data are presented in Table 1, and results are shown as concordia diagrams, probability density plots, and weighted mean ages (Fig. 5). The majority of data points plot close to concordia, indicating minimal Pb-loss, and are thus considered reliable for age determination.

The Landaran sample yielded a weighted mean 206Pb/238U age of 102 ± 0.6 Ma (n=19, MSWD = 6.3), with individual ages ranging from 98.5 to 121.7 Ma (Table 1 and Fig. 5a). The Bardashkand sample returned a weighted mean 206Pb/238U age of 104.2 ± 0.9 Ma (n=20, MSWD = 6.3), with ages spanning from 100.7 to 118.9 Ma (Table 1 and Fig. 5b). For Kuhsakht sample, the weighted mean 206Pb/238U age is 100.2 ± 0.8 Ma (n=20, MSWD = 6.4.7), and the ages range from 94.1 to 140.0 Ma (Table 1 and Fig. 5c). Finally, the Siabkuh sample yielded a weighted mean 206Pb/238U age of 99.6 ± 1.6 Ma (n=21, MSWD = 4.2), with individual ages ranging from 91.7 to 118.0 Ma (Table 1 and Fig. 5d). Notably, the MSWD values associated with the concordia ages differ markedly between samples, spanning from 0.48 to 150 (Fig. 5).

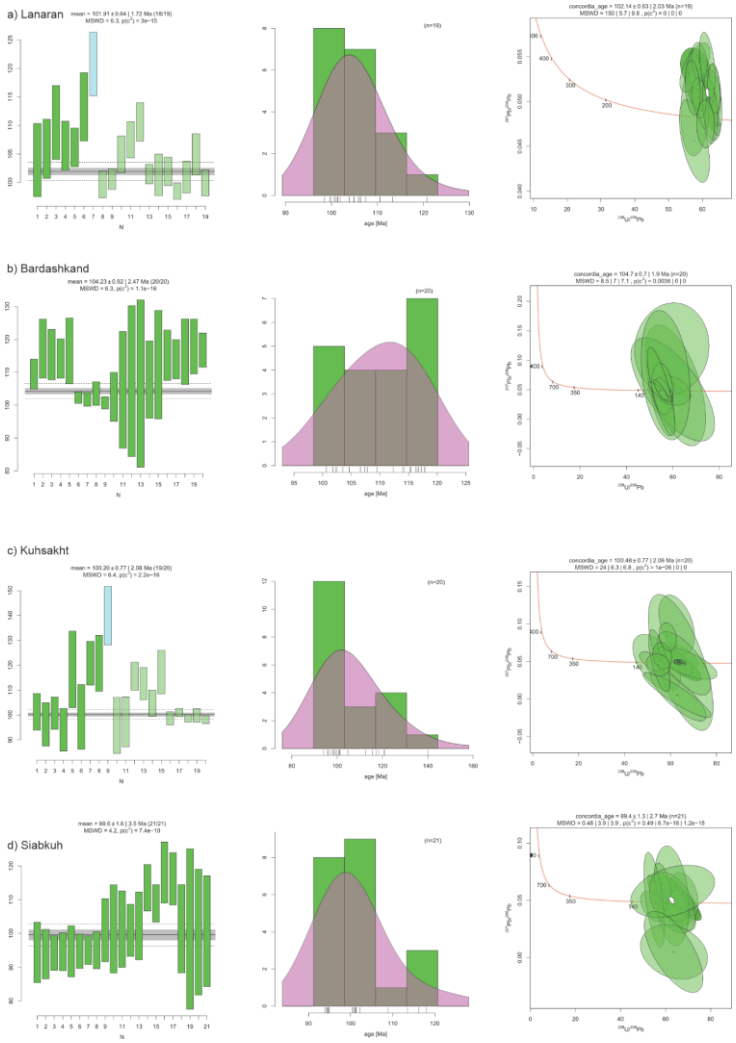

Figure 5. In-situ zircon U–Pb geochronological plots for the studied tuffaceous units from the southern Sabzevar subzone, including (a) Landaran, (b) Bardashkand, (c) Kuh-Sakht, and (d) Siabkuh prospects. For each sample, the plots show (left) the weighted mean 206Pb/238U age with 2σ uncertainty bars (the gray horizontal band represents the calculated weighted mean age and its 95%confidence level; rejected analyses are highlighted), (middle) Kernel Density Estimation (KDE) plot and age histogram, and (right) Tera–Wasserburg inverse Concordia diagram showing individual analytical error ellipses with a 2σ level of confidence and the resulting Concordia age.

The elevated MSWD values observed across the samples reflect geological heterogeneity within the zircon populations rather than analytical artifacts (Keller et al., 2018; Ruiz et al., 2022). Age histograms and kernel density estimation (KDE) plots reveal a dominant mid-Cretaceous cluster (~100 Ma) corresponding to the eruption and deposition of the tuff units, accompanied by a subordinate population of older grains (up to ~122 Ma, with a single grain in the Kuhdasht sample yielding ~140 Ma). These older grains are interpreted as inherited or xenocrystic zircons entrained from pre-existing crustal basement during magma ascent (e.g. Yang et al., 2007). To maintain transparency and capture the full complexity of the magmatic system, all analyses were retained. Consequently, the weighted mean 206Pb/238U ages of the primary, younger clusters provide the most robust constraint on the timing of volcanism and deposition.

Table 1. LA-ICP-MS U–Pb isotopic data for zircons from the studied samples. Abbreviations: SVL, Landaran; SVB, Bardashkand; SVK, Kuhsakht; SVS, Siabkuh.

Sample No.	Th/U	Pb207/Pb206	± 1σ	Pb207/U235	± 1σ	Pb206/U238	± 1σ	Rho	206Pb*/238U age	± (Ma) 1σ
SVL-1	0.54	0.16719	0.0121	0.12761	0.005	0.01725	0.0005	0.90	103.9	6.4
SVL-2	0.33	0.21007	0.0062	0.12190	0.005	0.01698	0.0004	0.81	105.9	5.2
SVL-3	0.76	0.04885	0.0060	0.11743	0.006	0.01725	0.0005	0.48	110.5	6.5
SVL-4	0.59	0.05072	0.0041	0.12093	0.004	0.01709	0.0004	0.85	106.4	4.3
SVL-5	0.97	0.05039	0.0041	0.12006	0.006	0.01698	0.0004	0.84	106.1	3.4
SVL-6	0.5	0.04514	0.0059	0.10897	0.007	0.01734	0.0005	0.84	113.3	6.0
SVL-7	0.59	0.16773	0.0121	0.12824	0.003	0.01730	0.0005	0.75	121.7	5.3
SVL-8	0.6	0.05120	0.0014	0.11113	0.003	0.01574	0.0002	0.66	99.7	2.4
SVL-9	0.5	0.04822	0.0011	0.10471	0.003	0.01575	0.0002	0.84	100.6	1.8
SVL-10	0.61	0.05450	0.0011	0.12688	0.003	0.01692	0.0003	0.77	104.9	3.2
SVL-11	0.73	0.05049	0.0011	0.11758	0.003	0.01692	0.0003	0.72	107.5	3.2
SVL-12	0.51	0.05162	0.0015	0.12422	0.004	0.01749	0.0003	0.68	110.6	3.4
SVL-13	0.5	0.04839	0.0006	0.10579	0.002	0.01586	0.0001	0.51	101.5	1.7
SVL-14	0.67	0.04955	0.0018	0.10857	0.004	0.01589	0.0003	0.62	101.3	3.7
SVL-15	0.64	0.04830	0.0012	0.10615	0.003	0.01594	0.0002	0.41	101.9	2.5
SVL-16	0.65	0.05140	0.0009	0.11391	0.002	0.01607	0.0002	0.92	98.5	1.4
SVL-17	0.55	0.07189	0.0017	0.12112	0.005	0.01625	0.0003	0.75	100.9	2.8
SVL-18	0.67	0.04718	0.0012	0.10736	0.003	0.01641	0.0003	0.64	104.9	3.6
SVL-19	0.52	0.05142	0.0013	0.11170	0.003	0.01576	0.0002	0.62	99.9	2.3
SVK-1	0.28	0.07981	0.0230	0.10446	0.027	0.01582	0.0011	0.90	101.3	7.4
SVK-2	0.54	0.10520	0.0330	0.12621	0.021	0.01581	0.0009	0.80	96.2	8.7
SVK-3	0.59	0.04947	0.0091	0.10449	0.017	0.01575	0.0006	0.70	100.7	6.5
SVK-4	0.35	0.10857	0.0216	0.21846	0.041	0.01596	0.0008	0.62	94.1	8.6
SVK-5	0.65	0.07900	0.0370	0.12375	0.045	0.01853	0.0015	0.68	118.3	15.4
SVK-6	0.46	0.03367	0.0156	0.10431	0.086	0.01553	0.0014	0.72	99.2	13.0
SVK-7	1.03	0.05931	0.0125	0.12542	0.020	0.01889	0.0009	0.82	120.8	8.8
SVK-8	0.53	0.04782	0.0176	0.01051	0.031	0.01578	0.0012	0.81	120.8	11.3
SVK-9	0.78	0.05088	0.0315	0.01128	0.028	0.01591	0.0015	0.91	140.0	11.8
SVK-10	0.46	0.05071	0.0128	0.09858	0.025	0.01496	0.0012	0.84	95.8	11.3
SVK-11	0.52	0.04033	0.0144	0.09945	0.041	0.01518	0.0011	0.77	97.2	10.1
SVK-12	0.6	0.05057	0.0180	0.12794	0.046	0.01816	0.0006	0.73	115.6	5.7

Sample No.	Th/U	Pb207/Pb206	± 1σ	Pb207/U235	± 1σ	Pb206/U238	± 1σ	Rho	206Pb*/238U age	± (Ma) 1σ
SVK-13	0.54	0.05658	0.0074	0.14087	0.019	0.01774	0.0005	0.36	112.6	6.5
SVK-14	0.55	0.21029	0.0062	0.19444	0.020	0.01700	0.0004	0.45	104.8	5.3
SVK-15	0.8	0.04458	0.0062	0.11462	0.017	0.01832	0.0007	0.39	117.2	8.8
SVK-16	0.5	0.04996	0.0014	0.10733	0.003	0.01558	0.0002	0.75	98.7	2.7
SVK-17	0.55	0.04850	0.0009	0.10603	0.002	0.01585	0.0002	0.85	101.0	1.7
SVK-18	0.8	0.05040	0.0009	0.11018	0.002	0.01586	0.0002	0.90	98.7	1.5
SVK-19	0.62	0.04712	0.0011	0.10139	0.003	0.01560	0.0003	0.92	101.2	2.6
SVK-20	0.47	0.05017	0.0008	0.10815	0.002	0.01563	0.0002	0.85	98.1	1.6
SVB-1	0.64	0.05086	0.0041	0.11973	0.010	0.01713	0.0004	0.72	108.6	3.8
SVB-2	0.54	0.04467	0.0062	0.11348	0.016	0.01835	0.0007	0.64	118.4	8.3
SVB-3	0.47	0.05030	0.0179	0.12577	0.045	0.01806	0.0006	0.33	115.3	7.5
SVB-4	0.7	0.04690	0.0098	0.11603	0.024	0.01787	0.0005	0.87	114.5	3.3
SVB-5	0.43	0.04636	0.0317	0.11707	0.080	0.01824	0.0008	0.65	116.7	8.0
SVB-6	0.58	0.04859	0.0012	0.10709	0.003	0.01599	0.0001	0.91	101.8	1.1
SVB-7	0.64	0.04889	0.0015	0.10725	0.003	0.01591	0.0002	0.62	101.5	2.0
SVB-8	0.73	0.04769	0.0031	0.10646	0.007	0.01619	0.0003	0.39	103.6	3.6
SVB-9	0.53	0.04779	0.0013	0.10371	0.003	0.01574	0.0002	0.28	100.7	1.9
SVB-10	0.76	0.05252	0.0099	0.11095	0.016	0.01603	0.0006	0.91	101.3	4.0
SVB-11	0.53	0.03329	0.0189	0.12911	0.101	0.01637	0.0014	0.62	103.6	14.8
SVB-12	0.83	0.14142	0.0559	0.27729	0.078	0.01679	0.0019	0.34	102.5	22.7
SVB-13	0.59	0.09228	0.0545	0.11563	0.093	0.01667	0.0021	0.75	106.1	18.9
SVB-14	0.41	0.07928	0.0250	0.11276	0.026	0.01686	0.0010	0.49	107.7	11.4
SVB-15	0.8	0.08887	0.0453	0.18100	0.113	0.01758	0.0013	0.37	110.9	15.8
SVB-16	0.62	0.05020	0.0179	0.12702	0.045	0.01803	0.0006	0.28	115.1	7.5
SVB-17	0.47	0.04681	0.0098	0.11720	0.025	0.01784	0.0005	0.67	114.1	4.8
SVB-18	0.74	0.04627	0.0317	0.11824	0.081	0.01820	0.0008	0.81	116.4	6.2
SVB-19	0.6	0.04556	0.0082	0.11800	0.022	0.01845	0.0007	0.91	118.9	4.3
SVB-20	0.49	0.04868	0.0080	0.12488	0.021	0.01828	0.0004	0.88	116.4	2.8
SVS-1	0.58	0.05451	0.0129	0.09732	0.017	0.01475	0.0007	0.90	94.4	5.2
SVS-2	0.58	0.04981	0.0084	0.09730	0.015	0.01467	0.0006	0.81	93.8	5.4
SVS-3	0.58	0.04817	0.0054	0.09668	0.008	0.01472	0.0004	0.63	94.3	4.8
SVS-4	0.74	0.05028	0.0069	0.09510	0.011	0.01478	0.0005	0.64	94.9	5.1
SVS-5	0.67	0.06056	0.0143	0.10509	0.020	0.01480	0.0006	0.39	94.4	7.5
SVS-6	0.8	0.04951	0.0051	0.09858	0.008	0.01480	0.0004	0.50	94.7	5.0
SVS-7	0.44	0.04740	0.0046	0.09749	0.009	0.01485	0.0003	0.60	95.1	3.9
SVS-8	0.63	0.04813	0.0065	0.09740	0.012	0.01485	0.0004	0.82	95.2	3.9
SVS-9	1.18	0.04325	0.0090	0.10544	0.022	0.01579	0.0008	0.63	100.9	8.3
SVS-10	0.45	0.07995	0.0230	0.10464	0.027	0.01585	0.0011	0.82	101.4	9.4
SVS-11	0.72	0.10538	0.0330	0.12642	0.021	0.01584	0.0009	0.91	94.5	6.4
SVS-12	0.44	0.04955	0.0091	0.10467	0.017	0.01578	0.0006	0.62	100.9	7.0
SVS-13	0.67	0.10875	0.0216	0.11883	0.041	0.01599	0.0008	0.39	101.8	9.7
SVS-14	0.76	0.05670	0.0075	0.13948	0.019	0.01777	0.0006	0.85	109.9	4.4

Sample No.	Th/U	Pb207/Pb206	± 1σ	Pb207/U235	± 1σ	Pb206/U238	± 1σ	Rho	206Pb*/238U age	± 1σ (Ma)
SVS-15	0.59	0.21074	0.0062	0.15252	0.019	0.01704	0.0004	0.67	105.3	4.6
SVS-16	0.49	0.04499	0.0063	0.11431	0.017	0.01848	0.0007	0.66	118.0	8.2
SVS-17	0.97	0.05066	0.0180	0.12668	0.045	0.01819	0.0006	0.65	115.9	6.2
SVS-18	0.68	0.07997	0.0230	0.10467	0.027	0.01585	0.0011	0.62	101.4	11.9
SVS-19	0.58	0.10541	0.0330	0.12646	0.021	0.01584	0.0019	0.39	104.8	23.0
SVS-20	0.48	0.04791	0.0231	0.01047	0.021	0.01570	0.0015	0.28	91.7	18.1
SVS-21	0.83	0.04905	0.0195	0.01075	0.032	0.01573	0.0013	0.67	114.0	14.5

4.4. Zircon trace-element characteristics

All analyzed zircon grains from the studied samples display Th/U ratios greater than 0.1, consistent with a magmatic origin (Hoskin and Black, 2000). Additionally, these zircons exhibit distinct patterns in rare earth element (REE) diagrams, characterized by a negative slope with low LaN/YbN ratios (<0.01) and enrichment in middle and heavy rare earth elements relative to light rare earth elements (Fig. 6). Such REE patterns serve as further evidence for the magmatic affinity of the studied zircons, as opposed to hydrothermal alteration or metamorphic processes, which typically result in enrichment of light rare earth elements and lower MREE/LREE ratios (Hoskin, 2005; Fig. 7a).

The U/Yb ratio in zircon crystals is widely used as a discriminator between zircons of continental and oceanic crust origin (Grimes et al., 2007). Low U/Yb ratios (~0.1) appear to be a reliable criterion for distinguishing zircons crystallized from fractionated melts of depleted MORB-type mantle, whereas other geological sources typically yield higher U/Yb ratios and require additional discrimination criteria (Grimes et al., 2015). Zircons crystallized in oceanic crust settings are characteristically enriched in Y, and heavy rare earth elements (HREE), and comparatively depleted in U and Th, relative to their counterparts formed in continental settings (Grimes et al., 2007). As illustrated in Figs. 7b and 7c, zircon crystals from the studied samples display variable ratios of these elements. Zircons from the Bensbord sample plot within the continental zircon field, whereas those from the other samples exhibit the geochemical signature of zircons crystallized in oceanic crust.

Zircons formed in arc-related settings are distinguished from their intraplate continental counterparts by higher Th/Nb and Hf/Th ratios (Deng et al., 2019). In the studied samples, most zircon grains display ratios comparable to those of arc-related zircons, with the exception of a few grains from the Landaran sample (Fig. 7d).

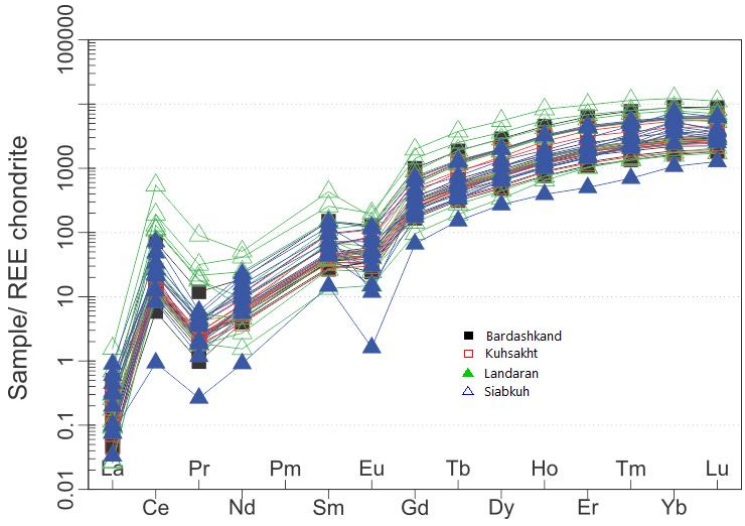

Figure 6. Chondrite-normalized rare earth element (REE) distribution patterns of analyzed zircon grains from the studied tuffs in the Bardashkand, Kuh-Sakht, Landaran, and Siabkuh prospects. The patterns display a steep positive slope with significant enrichment in

HREE relative to LREE, pronounced positive Ce anomalies (Ce/Ce*), and prominent negative Eu anomalies (Eu/Eu*), characteristic of primary, undisturbed magmatic zircons. Chondrite normalizing values are from Sun and McDonough (1989).

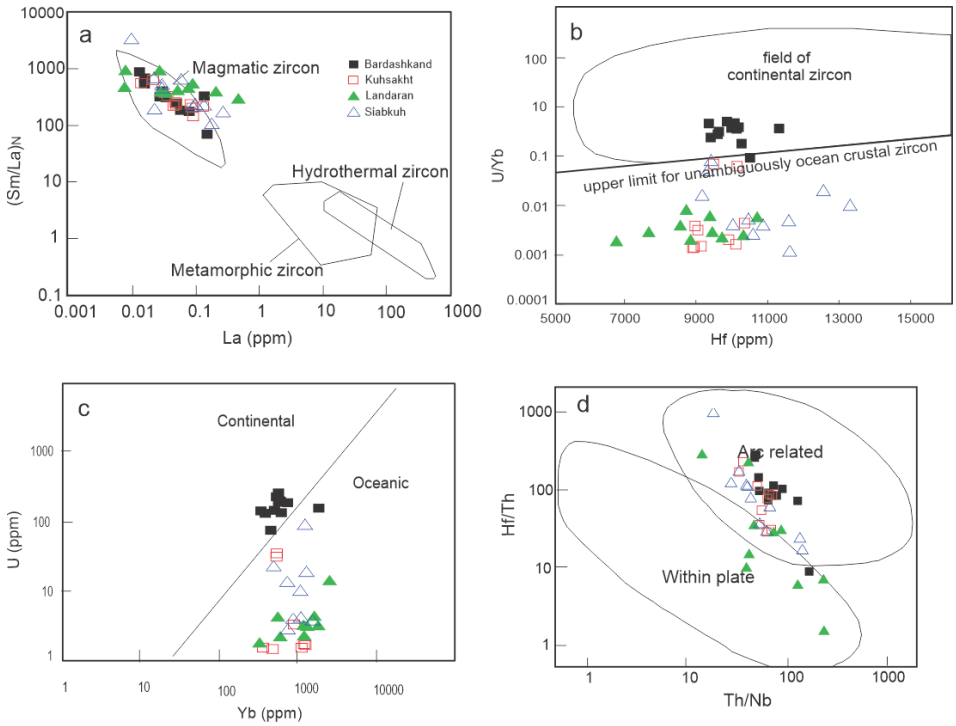

Figure 7. Trace- and minor-element discrimination diagrams for zircon grains from the studied samples: (a) La vs. $(Sm/La)_N$ diagram distinguishing unaltered magmatic zircons from hydrothermal/altered zircons (Hoskin, 2005); (b and c) Discrimination diagrams for continental crust vs. oceanic crust zircons (Grimes et al., 2007); (d) Th/Nb vs. Hf/Th diagram discriminating zircons formed in magmatic arc (subduction-related) environments from those formed in within-plate tectonic settings (Yang et al., 2012).

Table 2. Trace element concentrations (in ppm) of zircon grains from the studied samples. Abbreviations: SVL, Landaran; SVB, Bardashkand; SVK, Kuhsakht; SVS, Siabkuh.

Sample No.	Sc	Ti	Sr	Y	Nb	La	Ce	Pr	Nd	Sm	Eu	Gd
SVB-1	23.91	8.46	0.30	2122.56	1.06	0.16	11.19	0.28	2.78	6.82	2.36	60.95
SVB-2	26.20	18.56	0.68	1315.97	0.65	0.02	4.76	0.12	2.39	5.20	2.64	43.22
SVB-3	21.10	17.18	0.34	1510.99	0.78	0.03	7.11	0.18	2.51	5.56	2.51	47.50
SVB-4	20.70	15.51	0.24	2134.54	1.08	0.02	10.88	0.27	3.31	6.58	2.59	63.20
SVB-5	23.97	9.37	0.36	1787.05	0.99	0.01	13.57	0.34	2.78	6.78	1.78	57.54
SVB-6	21.33	18.53	0.27	2040.35	1.17	0.06	9.16	0.23	3.29	6.82	3.13	62.14
SVB-7	24.68	14.62	0.27	2356.34	1.33	0.03	8.08	0.20	2.68	7.00	3.37	70.90
SVB-8	21.24	19.63	0.24	2949.11	1.73	0.08	11.68	0.29	4.10	9.25	4.33	90.76
SVB-9	19.72	14.67	0.46	2512.73	1.48	0.04	11.95	0.30	3.62	7.18	2.79	71.62
SVB-10	23.38	15.43	0.30	2243.33	1.42	0.03	10.84	0.27	3.80	7.81	3.23	72.37
SVB-11	20.23	19.37	0.43	2519.44	1.61	0.05	9.42	0.24	3.92	8.13	3.80	83.31
SVB-12	59.49	10.61	0.50	7673.14	5.01	0.14	58.12	1.45	11.33	29.32	9.51	259.26
SVK-1	19.29	11.88	0.36	2216.52	1.46	0.05	12.12	0.30	3.17	6.47	2.56	65.39
SVK-2	21.35	24.72	0.42	4095.38	2.45	0.09	13.52	0.34	4.49	12.80	6.05	129.36

Sample No.	Sc	Ti	Sr	Y	Nb	La	Ce	Pr	Nd	Sm	Eu	Gd
SVK-3	21.69	17.82	0.45	2329.20	1.49	0.05	10.32	0.26	3.79	7.89	3.63	79.72
SVK-4	19.13	12.67	0.30	2221.32	1.47	0.05	11.75	0.29	3.56	7.69	3.04	64.57
SVK-5	18.84	13.79	0.32	2517.86	1.77	0.04	12.69	0.32	3.60	7.65	3.20	72.52
SVK-6	18.16	21.91	0.53	4120.07	3.28	0.09	13.64	0.34	4.65	8.78	4.09	106.92
SVK-7	29.37	20.51	0.53	2039.66	1.48	0.02	9.77	0.24	3.94	8.55	3.82	71.26
SVK-8	19.59	24.11	0.35	5383.91	3.88	0.09	17.66	0.44	5.49	11.91	6.18	156.60
SVK-9	29.18	21.81	0.32	5153.09	3.82	0.14	20.79	0.52	6.65	18.30	8.14	180.44
SVK-10	20.83	14.53	0.37	1619.38	1.18	0.01	9.16	0.23	2.29	5.36	2.20	47.49
SVL-1	19.59	11.76	0.38	1390.20	1.11	0.01	8.70	0.22	1.63	5.14	1.80	37.10
SVL-2	34.26	5.51	0.30	4821.22	4.11	0.03	87.49	2.19	5.76	15.28	2.94	145.43
SVL-3	32.36	25.94	0.36	5352.68	4.37	0.08	22.54	0.56	7.84	21.74	10.08	196.04
SVL-4	45.65	34.03	0.50	2340.98	2.64	0.04	20.74	0.52	3.15	7.61	3.74	72.49
SVL-5	54.74	33.80	0.43	2528.43	3.26	0.03	26.62	0.67	2.75	7.20	3.83	76.86
SVL-6	59.48	18.77	0.06	6723.07	9.22	0.09	104.73	2.62	14.71	29.96	8.76	233.56
SVL-7	88.75	12.22	0.05	13467.00	16.03	0.48	440.73	11.02	30.54	83.99	12.91	510.51
SVL-8	38.10	17.09	0.05	1152.16	2.35	0.01	9.15	0.23	0.93	2.60	1.10	24.74
SVL-9	61.90	23.75	0.01	8118.47	12.38	0.22	154.79	3.87	24.61	49.96	14.69	369.42
SVL-10	80.28	16.65	0.07	5171.98	9.32	0.05	91.27	2.28	4.02	13.74	4.43	146.33
SVS-1	58.00	9.08	0.06	3951.08	3.38	0.28	58.09	0.73	13.70	28.53	8.93	120.51
SVS-2	38.19	7.60	0.09	3039.53	2.68	0.01	18.23	0.42	9.31	18.33	0.87	81.68
SVS-3	53.76	5.58	0.13	1934.34	2.34	0.19	18.23	0.55	6.02	11.85	3.00	50.06
SVS-4	19.62	9.89	0.01	782.36	0.64	0.02	0.75	0.03	0.55	2.85	0.12	17.19
SVS-5	21.76	7.67	0.01	2065.15	2.30	0.10	38.93	0.49	8.02	14.11	5.28	60.15
SVS-6	25.95	25.75	0.01	2953.01	2.86	0.06	26.99	0.64	11.74	23.79	3.58	97.75
SVS-7	33.89	11.43	0.04	2622.38	3.43	0.03	17.30	0.23	4.42	9.62	2.21	55.11
SVS-8	27.97	13.91	0.01	1976.57	2.54	0.03	6.63	0.14	3.32	8.36	1.09	45.22
SVS-9	30.25	21.13	0.55	2100.85	1.53	0.02	10.06	0.25	4.06	8.81	3.93	73.40
SVS-10	20.18	24.84	0.36	5545.43	3.99	0.09	18.19	0.45	5.66	12.27	6.36	161.30
SVS-11	30.05	22.47	0.33	5307.68	3.94	0.14	21.42	0.54	6.85	18.85	8.38	185.86

Table 2 (continued)

Sample No.	Tb	Dy	Ho	Er	Tm	Yb	Lu	Hf	Ta	Pb	Th	U
SVB-1	22.32	243.47	89.68	396.09	73.83	577.86	94.19	11266.27	0.78	0.35	133.21	200.13
SVB-2	14.83	156.68	54.76	230.08	43.58	344.35	58.68	9296.60	0.40	0.19	31.93	149.84
SVB-3	16.24	175.26	64.37	262.56	51.15	390.55	62.68	9929.17	1.47	1.03	36.82	138.22
SVB-4	22.17	246.59	87.35	376.10	71.35	542.35	87.81	10019.33	0.29	1.40	78.54	240.85
SVB-5	20.40	214.81	77.14	328.94	60.60	458.94	72.05	10214.95	0.40	1.41	87.54	78.21
SVB-6	22.13	239.24	85.83	352.74	66.74	511.27	83.33	9579.90	0.45	2.87	60.29	152.74
SVB-7	23.88	256.43	94.23	394.65	73.71	580.46	94.47	10132.50	0.28	2.60	103.98	212.94
SVB-8	32.05	344.50	126.21	523.20	98.63	748.25	121.08	9547.10	0.32	2.50	111.38	197.26
SVB-9	24.55	270.13	103.41	426.14	80.90	608.43	96.70	10074.58	0.43	0.57	95.84	207.12
SVB-10	24.78	265.06	93.22	404.17	77.29	574.92	93.30	9804.57	0.72	0.66	100.16	273.91
SVB-11	28.42	305.74	108.68	443.75	83.49	623.74	104.35	9349.92	1.43	0.70	84.70	141.05
SVB-12	88.70	930.30	325.68	1336.65	250.92	1869.37	284.75	10453.41	2.24	0.94	821.69	164.46
SVK-1	22.68	239.49	91.88	381.96	71.88	542.62	88.63	10090.80	1.88	1.29	103.18	32.20
SVK-2	43.23	445.06	159.16	662.26	119.63	906.53	142.84	8915.89	0.92	2.23	135.20	3.30
SVK-3	26.03	270.41	96.59	404.34	73.80	546.90	89.24	9430.12	0.59	0.75	74.75	36.00
SVK-4	21.53	244.04	92.64	380.67	70.64	527.84	87.10	9859.71	0.46	1.43	97.33	1.02
SVK-5	26.20	286.43	104.85	437.23	82.95	633.46	105.51	10060.33	1.38	0.49	111.52	0.98
SVK-6	41.25	487.86	188.56	811.43	151.17	1129.40	182.54	8887.58	0.30	0.34	226.31	1.51
SVK-7	23.18	235.89	84.45	335.33	64.39	484.03	79.16	8994.75	0.95	0.55	49.04	1.45
SVK-8	56.74	620.52	228.87	941.41	172.18	1263.88	201.38	8850.19	1.72	0.76	240.80	1.66
SVK-9	60.06	624.34	221.02	887.97	163.71	1212.56	191.71	9087.95	1.70	2.97	202.56	1.71
SVK-10	15.80	166.44	63.08	250.19	49.10	365.75	58.50	10301.58	1.52	1.48	42.66	1.52
SVL-1	13.03	143.43	53.81	217.78	43.19	330.82	55.32	10657.50	0.80	16.66	45.66	1.72
SVL-2	54.39	602.04	220.05	906.66	168.77	1200.87	170.94	9400.50	0.69	11.46	932.78	3.10
SVL-3	63.72	652.91	224.37	895.59	166.50	1219.38	195.68	8792.14	0.60	6.51	203.64	2.18
SVL-4	24.68	260.95	96.97	401.34	74.48	564.46	91.84	8670.18	0.24	0.80	228.84	4.09
SVL-5	27.20	290.15	104.55	437.02	81.23	605.68	98.96	8503.95	2.12	1.33	238.31	2.11
SVL-6	90.31	909.81	302.56	1221.24	229.13	1642.97	228.23	7620.53	3.21	3.25	384.08	4.20
SVL-7	178.47	1764.79	598.00	2041.03	369.96	2562.89	357.82	9331.90	1.23	2.59	3679.92	13.89
SVL-8	9.13	108.40	46.58	214.03	45.60	368.42	67.50	9675.27	0.19	2.72	33.55	0.74
SVL-9	119.73	1160.96	403.25	1436.19	258.10	1838.14	262.44	6713.76	0.40	1.33	485.52	3.06
SVL-10	55.07	586.49	216.28	915.07	175.10	1336.07	211.66	10272.12	1.30	0.80	1177.09	2.99
SVS-1	35.64	426.42	136.99	621.09	148.32	1565.60	201.88	10541.02	1.06	0.27	473.80	3.65
SVS-2	26.47	336.81	116.39	474.83	109.18	1109.31	124.63	9977.61	0.92	3.25	74.06	4.02
SVS-3	16.38	207.03	72.62	304.88	77.97	883.74	104.03	11542.18	0.87	2.26	94.14	3.86
SVS-4	7.20	87.02	28.16	105.31	22.64	224.25	40.98	10411.68	0.22	3.33	11.79	1.06
SVS-5	18.03	217.33	74.06	314.15	72.51	754.99	102.18	10822.21	0.75	0.98	153.47	2.70
SVS-6	28.53	351.23	112.27	448.05	94.86	933.18	118.45	11573.08	0.93	1.06	380.07	0.99
SVS-7	19.88	258.53	94.55	418.18	100.53	1089.74	130.81	13261.25	1.23	1.34	148.32	9.85
SVS-8	15.76	203.94	72.20	305.91	71.48	741.60	90.74	12512.44	1.02	1.61	99.19	13.30
SVS-9	23.88	242.97	86.99	345.39	66.33	498.55	81.53	9264.60	0.98	0.57	50.51	22.50
SVS-10	58.45	639.14	235.74	969.65	177.35	1301.79	207.42	9115.69	1.77	0.78	248.03	18.60

Sample No.	Tb	Dy	Ho	Er	Tm	Yb	Lu	Hf	Ta	Pb	Th	U
SVS-11	61.86	643.07	227.65	914.61	168.62	1248.93	197.47	9360.58	1.75	3.06	208.64	90.36

4.5. Tectonomagmatic evolution and metallogenic implications

The manganese occurrences in southern Sabzevar have traditionally been interpreted as exhalative and Besshi-type volcanogenic massive sulfide (VMS) systems developed within a back-arc basin setting (Maghfouri et al., 2016, 2017). Our new U–Pb zircon geochronology yields depositional ages clustering around ca. 100 Ma for the tuffaceous units closely associated with these Mn mineralizations. Subordinate older zircon populations identified within these tuffs likely represent inherited or xenocrystic grains recycled from pre-existing magmatic foundations. This ~100 Ma depositional pulse fits well into the broader regional magmatic framework; published radiometric data from southern Sabzevar magmatic suites indicate protracted Late Cretaceous igneous pulses spanning ca. 100 to 75 Ma (Kazemi et al., 2019; Mazhari et al., 2019). Furthermore, chronological and geochemical constraints on pillow lavas and sheeted dikes from the Sabzevar ophiolite complex reveal episodic crystallization between ~113 and 90 Ma, reflecting diverse alkaline, calc-alkaline, and tholeiitic magmatic suites across a broad geodynamic continuum from oceanic intraplate volcanism to forearc systems (Mazhari and Bea, 2026). Direct physical evidence of seafloor hydrothermal discharge is documented in the Arghash area within the eastern Sabzevar sub-zone, where spilitic alteration, pervasive pyrite mineralization, extensive malachite staining, and fossil hydrothermal vent/chimney-like structures demonstrate sustained hydrothermal circulation within the basaltic oceanic crust (Alaminia and Mazhari, 2026). These field and geochemical observations strongly corroborate an exhalative hydrothermal regime, reinforcing the genetic classification of the regional Mn mineralizations within a Besshi-type VMS framework.

Zircon trace-element compositions from the studied tuffs provide critical insights into the ambient tectonic regime. Discrimination diagrams confirm that the majority of the zircon grains reflect an oceanic crustal provenance, whereas the Bardashkand samples display a discernible continental crust signature. Tectonically, most grains exhibit signatures indicative of an arc/subduction-related environment, accompanied by a subordinate population displaying within-plate affinities (Figs. 7c, d).

Synthesizing the chronostratigraphic, geochemical, and metallogenic data reveals that hydrothermal exhalative Mn mineralization in southern Sabzevar culminated at around 100 Ma in an active oceanic realm. Rather than reflecting a simple isolated back-arc basin, the juxtaposition of predominant arc-related signatures, subordinate within-plate geochemical components, and local continental contributions is most consistent with an evolving accretionary wedge–forearc–arc system, in line with geodynamic models proposed by Rezaei et al. (2018) and Mazhari and Bea (2026). In this geodynamic setting, subduction initiation and associated extensional rifting fostered the high geothermal gradients, convective seawater circulation, and crustal permeability required to trigger exhalative hydrothermal venting and precipitate Besshi-type Mn–(Fe–Cu) horizons.

5. Conclusions

Integrated zircon U–Pb geochronology and trace-element geochemistry of tuffaceous rocks intimately associated with the manganese deposits in southern Sabzevar provide robust constraints on the timing of volcanosedimentary accumulation and its geodynamic setting. Zircon crystallization ages define a coherent maximum depositional age of ca. 100 Ma for the volcaniclastic successions. This constrains the hydrothermal exhalative Besshi-type Mn mineralization to the mid-Cretaceous (Cenomanian–Albian boundary), directly linking ore formation to a major regional pulse of subaqueous magmatism. The presence of subordinate older inherited and xenocrystic zircons records the thermal reworking and incorporation of earlier Mesozoic magmatic crustal components during basin evolution.

Zircon trace-element discrimination systematics demonstrate that the parental melts were predominantly derived from an oceanic crustal regime within a subduction-related arc system, accompanied by localized within-plate signatures and, in the case of the Bardashkand sector, recognizable continental crustal involvement. Together with documented field evidence of fossil

hydrothermal chimneys, spilitic alteration, and pervasive base-metal mineralizations in the adjacent crustal sections, these data delineate an evolving accretionary wedge–forearc–arc setting rather than a simple, isolated back-arc basin. In this tectonic environment, extensional rifting coupled with elevated mantle thermal anomalies facilitated intense convective hydrothermal circulation within the permeable basaltic-volcaniclastic crust, ultimately focusing exhalative venting and precipitating stratiform Mn horizons onto the paleo-seafloor.

Acknowledgements

We are truly grateful to the Editor-in-Chief and the two anonymous reviewers for their thoughtful evaluations and insightful critiques, which proved invaluable in refining the arguments and enhancing the overall clarity of this work.

Declarations

Data and code availability

The geochemical and geochronological datasets supporting the findings of this study can be obtained from the corresponding author upon reasonable request. This research did not rely on any proprietary code or automated computational algorithms.

Conflicts of interest

The authors certify that they have no financial interests, institutional affiliations, or personal associations that could be perceived as having influenced the objectivity of the results presented here.

Ethical approval

The investigation adheres strictly to recognized academic ethical norms. Furthermore, the authors confirm that this manuscript represents original research and is neither currently submitted elsewhere nor previously published in any peer-reviewed venue.

References

Alaminia, Z., & Mazhari, S. A. (2026). Geochemistry and metallogenic significance of pillow lavas associated with Cretaceous mafic intrusive bodies in the Arghash area, East of Sabzevar. Petrological Journal. doi: 10.22108/ijp.2026.149131.1388

Belousova, E. A., Griffin, W. L., O'Reilly, S. Y., & Fisher, N. J. (2002). Igneous zircon: trace element composition as an indicator of source rock type. Contribution to Mineralogy and Petrology, 143, 602–622. https://doi.org/10.1007/s00410-002-0364-7

Broska, I., & Petrik, I. (2014). Accessory phases in genesis of igneous rocks. In S. Kumar and R. N. Singh (Eds.), Modelling of magmatic and applied processes (pp. 109–149). Springer International Publishing.

Brlek, M., Gaynor, S. P., Mongelli, G., Bauluz, B., Sinisi, R., Brčić, V., … & Schaltegger, U. (2021). Karst bauxite formation during Miocene Climatic Optimum (central Dalmatia, Croatia): mineralogical, compositional and geochronological perspectives. International Journal of Earth Sciences, 110(8), 2899–2922.

Calver, C. R., Cumming, G. V., Halverson, G. P., Crowley, J. L., Roberts, N. J., & Schmitz, M. (2026). High-resolution U-Pb dating of the Croles Hill Diamictite, Tasmania: Near-synchroneity of widely separated mid-Ediacaran glacial deposits. Precambrian Research, 432, 107958.

Chakraborty, P. P., Sharma, R., Das, K., Sharma, A., & Saha, S. (2023). U-Pb zircon geochronology of volcaniclastics and encasing sandstones from the Chhoti Khatu section: Bearing on the Neoproterozoic Marwar Supergroup stratigraphy and its global implications. Geosystems and Geoenvironment, 2(1), 100111.

Christin Natalia, H., Widiyawati, Jati Widiatama, A., Naufan Hendrawan, R., Ananda Gita Christi, D., Tri Kemala, A., & Nur Faqih An Nahar, R. (2024). Distribution of Manganese Ore Deposit in Sukaagung Village, Tanggamus Regency, Lampung. IOP Conference Series: Earth and Environmental Science (Vol. 1378, No. 1, p. 012026). IOP Publishing.

Deng, C., Sun, G., Sun, D., Han, J., Yang, D., & Tang, Z. (2019). Morphology, trace elements, and geochronology of zircons from monzogranite in the Northeast Xing'an Block, northeastern China: constraints on the genesis of the host magma. Mineralogy and Petrology, 113(5), 651–666.

Grimes, C. B., John, B. E., Kelemen, P. B., Mazdab, F., Wooden, J. L., Cheadle, M. J., Hanghøj, K., & Schwartz, J. J. (2007). The trace element chemistry of zircons from oceanic crust: a method for distinguishing detrital zircon provenance. Geology, 35, 643–646. https://doi.org/10.1130/G23603A.1

Grimes, C. B., Wooden, J. L., Cheadle, M. J., & John, B. E. (2015). Fingerprinting tectono-magmatic provenance using trace elements in igneous zircon. Contribution to Mineralogy and Petrology, 170, 1–26. https://doi.org/10.1007/s00410-015-1199-3

Guo, X., Lu, Y., Zhang, Q., Ren, J., & Cai, W. (2024). The geological characteristics, resource potential, and development status of manganese deposits in Africa. Minerals, 14(11), 1088.

Hashempour, S. S., Maghfouri, S., Rastad, E., & Gonzalez, F. J. (2023). Mohammadabad Manganese deposit, southwest Sabzevar basin, Iran: evidence of sea-floor exhalation and geochemical studies in the late Cretaceous volcano-sedimentary sequence. Journal of Geochemical Exploration, 245, 107127.

Hoskin, P. W. O., & Black, L. P. (2000). Metamorphic zircon formation by solid-state recrystallization of protolith igneous zircon. Journal of Metamorphic Geology, 18(4), 423–439. https://doi.org/10.1046/j.1525-1314.2000.00266.x

Hoskin, P. W. O. (2005). Trace-element composition of hydrothermal zircon and the alteration of Hadean zircon from the Jack Hills, Australia. Geochimica et Cosmochimica Acta, 69, 637–648. https://doi.org/10.1016/j.gca.2004.07.006

Jafari, A., & Ghasemi, H. (2023). Geologic history of the Sabzevar oceanic Basin, NE Iran: An overview from continental rifting to obduction in the Neo-Tethys oceanic system. Journal of Asian Earth Sciences, 245, 105559. https://doi.org/10.1016/j.jseaes.2023.105559

Karataş, B., Akyildiz, M., Yildirim, N., & Yildirim, E. (2022). The origin of manganese formations at Çağalali Hill and Kevrikevr Hill related to the late Triassic rifting of the South Neotethys, SE Turkey: The geological, mineralogical and geochemical components. Journal of African Earth Sciences, 186, 104421.

Kazemi, Z. (2018). Petrology, geochemistry and tectonic model of Late Cretaceous magmatism in northern edge of the central Iran zone (Southwest of Sabzevar) [Doctoral dissertation, Shahrood University of Technology]. [In Persian].

Kazemi, Z., Ghasemi, H., Tilhac, R., Griffin, W., Moghadam, H. S., O'Reilly, S., & Mousivand, F. (2019). Late Cretaceous subduction-related magmatism on the southern edge of Sabzevar basin, NE Iran. Journal of the Geological Society, 176(3), 530–552.

Keller, C. B., Schoene, B., & Samperton, K. M. (2018). A stochastic sampling approach to zircon eruption age interpretation. Geochemical Perspectives Letters.

Khalatbari Jafari, M., Babaie, H., & Gani, M. (2013). Geochemical evidence for Late Cretaceous marginal arc-to-backarc transition in the Sabzevar ophiolitic extrusive sequence, northeast Iran. Journal of Asian Earth Sciences, 70–71, 209–230.

Königer, S., Lorenz, V., Stollhofen, H., & Armstrong, R. A. (2002). Origin, age and stratigraphic significance of distal fallout ash tuffs from the Carboniferous–Permian continental Saar–Nahe Basin (SW Germany). International Journal of Earth Sciences, 91(2), 341–356.

Liang, J. L., Ding, X., Sun, X. M., Zhang, Z. M., Zhang, H., & Sun, W. D. (2009). Nb/Ta fractionation observed in eclogites from the Chinese Continental Scientific Drilling Project. Chemical Geology, 268, 27–40.

Maghfouri, S., Rastad, E., Mousivand, F., Lin, Y., & Zaw, K. (2016). Geology, ore facies and sulfur isotopes geochemistry of the Nudeh Besshi-type volcanogenic massive sulfide deposit, southwest Sabzevar basin, Iran. Journal of Asian Earth Sciences, 125, 1–21.

Maghfouri, S., Rastad, E., Mousivand, F., Choulet, F., & Ye, L. (2017). Geological and geochemical constraints on the Cheshmeh-Frezi volcanogenic stratiform manganese deposit, southwest Sabzevar basin, Iran. Ore Geology Reviews, 89, 96–113.

Maghfouri, S., Rastad, E., Momenzadeh, M., Movahednia, M., Hashempour, S. S., Amini Jadehkenary, K.,

… & Aghamolaei, K. (2026). Malayer–Esfahan Metallogenic Belt, Iran: Jurassic–Early Cretaceous sediment–(volcanic)-hosted Zn–Pb (±Ba±Ag), Fe–Mn–Pb (±Ba±Cu) and Ba (±Pb±Zn) deposits with evolution of basin. Journal of the Geological Society, 183(1), jgs2024-284.

Mazhari, S. A., & Bea, F. (2026). Petrogenesis and tectonomagmatic evolution of the Sabzevar ophiolitic complex based on whole rock geochemistry, zircon U–Pb geochronology, and zircon trace element composition in pillow lavas and sheeted dikes of the Sultanabad area. Petrological Journal, 17(2), 95–130. doi: 10.22108/ijp.2026.139882.1332

Mazhari, S. A., & Klötzli, U. (2023). The composition of zircon trace elements in the various Cadomian granitoid types of Taknar zone, south of Sabzevar. Petrological Journal, 14(2), 89–116. doi: 10.22108/ijp.2023.136687.1293

Mazhari, S. A., Klötzli, U., & Safari, M. (2019). Petrological investigation of Late Cretaceous magmatism in Kaboodan area, NE Iran: Evidence for an active continental arc at Sabzevar zone. Lithos, 348, 105183.

Moghadam, S. H., Corfu, F., Chiaradia, M., Stern, R. J., & Ghorbani, G. (2014). Sabzevar Ophiolite, NE Iran: Progress from embryonic oceanic lithosphere into magmatic arc constrained by new isotopic and geochemical data. Lithos, 210–211, 224–241. https://doi.org/10.1016/j.lithos.2014.10.004

Moghadam, S. H., Xiao, W., Dilek, Y., et al. (2025). Mineral, bulk rock, and isotope geochemistry of the Late Cretaceous Sabzevar ophiolite in NE Iran and the magmatic and tectonic evolution of a continental back-arc basin oceanic crust. Geological Society of America Bulletin, 137(1–2), 649–681. https://doi.org/10.1130/B37690.1

Njinchuki, N. D., Njiosseu Tanko, E. L., Tsoungui, P. N. E., Kamguia, B. W., Nzepang Tankwa, M., Soh Tamehe, L., … & Nzenti, J. P. (2026). Zircon Trace Element Constraints on the Evolution of the Continental Crust in the Western Domain of the Congo Craton. Minerals, 16(4), 414.

Omrani, H., Moazzen, M., & Oberhansli, R. (2018). Geodynamic evolution of the Sabzevar zone, northern central Iranian micro-continent. Mineralogy and Petrology, 112, 65–83.

Pupin, J. P. (2024). Zircon typology: a synthesis. Applications to magmatic, metamorphic and sedimentary rocks. Journal of Petrology, 65(11), egae111.

Putzolu, F., Armstrong, R. N., Benson, T. R., Boutt, D. F., Butler, K. L., Dolgopolova, A., … & Munk, L. A. (2025). Volcano-sedimentary deposits: Overview of an emerging type of lithium resource. Economic Geology, 120(3), 541–573.

Rezaei, Z., Noghreyan, M., & Saccani, E. (2018). Petrology and geochemistry of sheeted dykes and pillow lavas from the Sabzevar ophiolitic mélange (NE Iran): New constraints for the Late Cretaceous evolution of the Neo-Tethys. Ofioliti, 43(2), 147–172. https://doi.org/10.4454/ofioliti.v43i2.461

Ruiz, M., Schaltegger, U., Gaynor, S. P., Chiaradia, M., Abrecht, J., Gisler, C., … & Wiederkehr, M. (2022). Reassessing the intrusive tempo and magma genesis of the late Variscan Aar batholith: U–Pb geochronology, trace element and initial Hf isotope composition of zircon. Swiss Journal of Geosciences, 115(1), 20.

Sun, S. S., & McDonough, W. F. (1989). Chemical and isotopic systematics of oceanic basalts: implications for mantle composition and processes. Geological Society, London, Special Publications, 42(1), 313–345.

Tashi, M., Mousivand, F., Ghasemi, H., Maghfouri, S., Maslennikov, V., Peter, J. M., & Sadykov, S. A. (2021). Evolution of the Garmab-e-Paein native copper-rich volcanogenic massive sulfide deposit from northeast Iran: Insights from sulfur isotope and chlorite chemistry. Ore Geology Reviews, 138, 104345.

Yang, J. H., Wu, F. Y., Wilde, S. A., Xie, L. W., Yang, Y. H., & Liu, X. M. (2007). Tracing magma mixing in granite genesis: in situ U–Pb dating and Hf-isotope analysis of zircons. Contributions to Mineralogy and Petrology, 153(2), 177–190.

Yang, J., Cawood, P. A., Du, Y., Huang, H., Huang, H., & Tao, P. (2012). Large Igneous Province and magmatic arc sourced Permian–Triassic volcanogenic sediments in China. Sedimentary Geology, 261, 120–131.

Zhong, S., Li, S., Seltmann, R., Lai, Z., & Zhou, J. (2021). The influence of fractionation of REE-enriched minerals on the zircon partition coefficients. Geoscience Frontiers, 12, 101094. https://doi.org/10.1016/j.gsf.2020.10.002